Selective wet oxidation of AlAsSb alloys on GaAs

Stéphane Calvez, Oleksandr Stepanenko, Kevin Louarn, Emmanuelle Daran, Alexandre Arnoult, Guilhem Almuneau

Selective wet oxidation of AlAsSb alloys on GaAs

STEPHANE CALVEZ,[1,*] OLEKSANDR STEPANENKO,[1] KEVIN LOUARN,[1] EMMANUELLE DARAN,[1] ALEXANDRE ARNOULT,[1] AND GUILHEM ALMUNEAU[1]

[1]*LAAS-CNRS, 7 avenue du Colonel Roche, F-31400 Toulouse, France*

**scalvez@laas.fr*

Abstract: In this paper, the oxidation of thin low-Sb-containing AlAsSb layers quasi-lattice matched on GaAs substrates is studied in detail since, compared to AlGaAs, these alloys had the prospects of being laterally oxidized at a faster rate, at lower process temperatures and with a reduced volume change. Combining monitoring data of the oxidation kinetics and anisotropy with atomic-force-microscopy surface measurements enables to establish the optimal composition range and process parameters that lead to nearly-isotropic and Sb-segregation-free oxidations. The study also shows that strain plays a central role in triggering the detrimental Sb segregation.

1. Introduction

The oxidation of aluminum-containing III-V semiconductors is a technological process primarily used to introduce optical and/or electrical confinements in opto-electronic devices including Vertical-Cavity Surface-Emitting Lasers [1,2], passive and active waveguide-based devices such as edge-emitting lasers [3], whispering-gallery-mode micro-resonators [4], photonic crystal [5] and nonlinear [6,7] waveguides. To-date, most of the reported material studies have been dedicated to the oxidation of AlGaAs compounds. They have provided a comprehensive dataset on its kinetics [3,8–10], on its compositional and structural selectivity [11–14], on its anisotropy [15–17] as well as on the structural properties of the resulting oxide [18–20]. Analysis of these data has revealed that this type of oxidation is a complex interplay between localized chemical reactions and the diffusion of the reactants and by-products through the oxide [21–23], the latter two mechanisms being further compounded by strain effects [24–27] arising from the volume shrinkage occurring during the transformation of the semiconductor into its corresponding oxide. Investigations

of the oxidation of other Al-containing III-V semiconductors have also been carried out to gain additional chemico-physical insight and to potentially expand the use of this process to make transistors or photonics devices operating in other spectral bands than the near-infrared window (800-1000 nm). So far, the studied alloys include AlIn(Ga)P [28] on GaAs, AlInAs [29–32] and AlAsSb [33–35] on InP, AlInN on GaN [36,37], and AlAsSb on GaSb [38–42].

In this paper, we report on the oxidation of AlAsSb compounds quasi-latticed-matched to GaAs with a view to provide experimental information on the influence on the process of alloying (and bi-axially straining) the to-be-oxidized layer with antimony rather than with gallium. This study complements the data presented in reference [43] as it focusses on samples with low Sb-content to limit the amount of antimony segregation [44].

2. Sample and process description

The samples used in this study consist of a 5-pair 50-nm GaAs/50-nm AlAs superlattice used to calibrate the growth rates and that is subsequently buried under 1 µm of GaAs, a 50-nm thick $AlAs_{1-x}Sb_x$ layer capped with 500-nm thick of GaAs.

The samples were grown by molecular beam epitaxy on (001)-oriented GaAs substrates using standard conditions for AlGaAs layers. The AlAsSb layers were grown using a V/III ratio of 3.2 and temperature of 580°C. We point out that the incorporation of the Sb into the AlAsSb layer depends nonlinearly on the flux of Sb_4 supplied by the valved cracker effusion cell. The composition and thickness of the $AlAs_{1-x}Sb_x$ layers were determined using fits of the High-Resolution X-Ray Diffraction (HR-XRD) measurements made around the GaAs (004) reflection peak and displayed in Fig. 1. The HR—XRD curves show a good structural quality of the grown AlAsSb layers with no indication of relaxation regardless the Sb composition. Narrow small satellites peaks on Fig. 1 originates from the underlying superlattice.

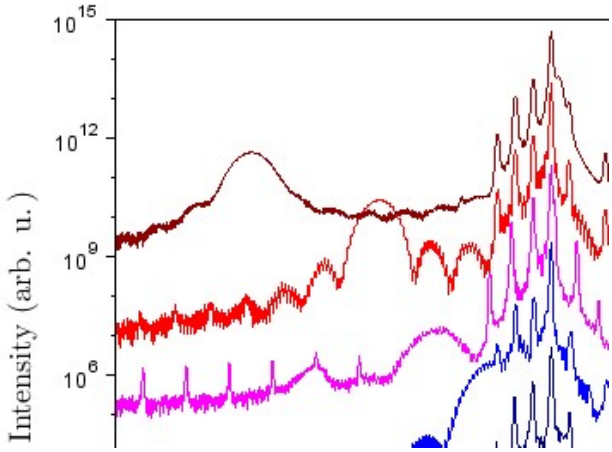

*Fig. 1. High-Resolution X-Ray Diffraction theta-2*theta scans of the as-grown samples, the angular reference being the (004) substrate reflection peak. The curves are deliberately shifted along the vertical axis by multiplication by a factor 100 for enhanced visibility.*

Sample processing started by defining 42-µm-side-square and 42-µm-diameter-circular mesas by contact lithography into SPR700 photoresist. These patterns were subsequently transferred into the III-V semiconductor multilayer using an isotropic wet etching solution (H_3PO_4/H_2O_2/DI water with 3/1/25 dilution ratio). The ~800-nm-deep etched sidewalls of these mesas give access to the AlAsSb layer for lateral oxidation upon resist removal. The wet oxidation was performed straightaway in a vacuum furnace commercialized by AlOxtec that provides uniform, controlled, and reproducible treatment of up-to-4-inch wafers. Its reduced pressure (500 mbar unless stated otherwise) chamber is supplied with an oxidizing atmosphere composed of water vapor (10 g/l) and N_2/H_2 (95%/5%) forming gas supplied at a flow rate of 0.6 l/min.

3. Measurement methods of the oxide aperture shape and oxidation-related volume change

The oxidation furnace is equipped with an *in-situ* micro-reflectometry-based imaging system [45] that is used to acquire the real-time monitoring data presented and analyzed hereafter. Typical top-view images recorded during the lateral oxidation of

an AlAs, $AlAs_{0.967}Sb_{0.033}$ or $AlAs_{0.866}Sb_{0.134}$ layer from circular etched mesas are presented in Fig. 2. On these images, the edge of the etched mesas is black and the so-called oxide apertures are the boundaries between the central light grey and the white areas that corresponds respectively to the (unoxidized) semiconductor and oxide zones.

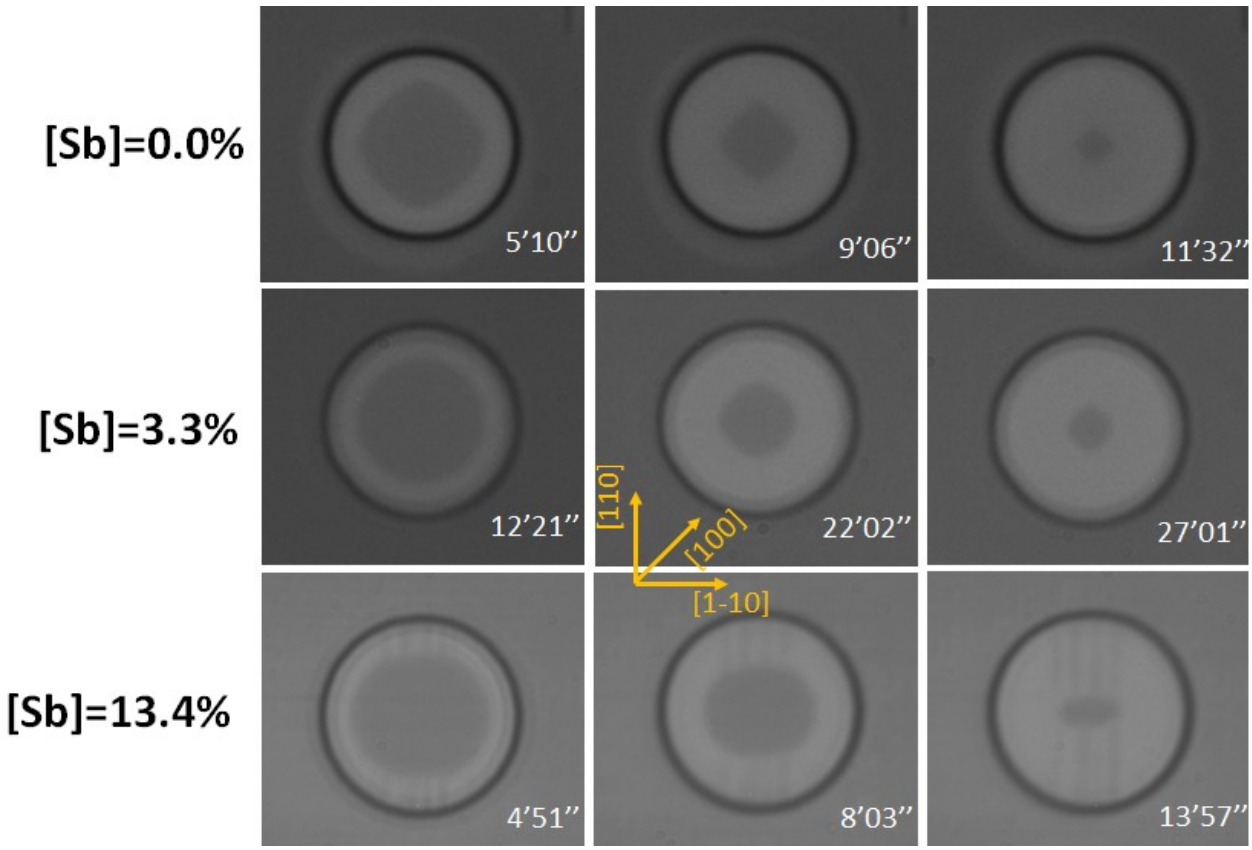

Fig. 2. Infrared microscopy images measured in-situ during the oxidation (at 420°C, 500 mbar) of 42µm-diameter circular mesas of AlAsSb with different Sb concentration.

As it can be observed in Fig. 2, the oxide aperture shape often differs from a scaled version of the mesa contour, the deformation being caused mostly by an anisotropy occurring during the oxidation process and by diffusion-based smoothing effects. The above-mentioned anisotropy can originate from a crystallographic dependence of the reactions [15,23], from an anisotropic diffusion of the reactants or of the by-products through the formed oxide, or from an uneven distribution of the oxide-induced strain field [26]. In this particular study, except for the $AlAs_{0.866}Sb_{0.134}$ layer and as already observed for AlGaAs-

layers on (001)-oriented substrates, the lateral oxidation of an AlAsSb layer from a circular (or a square) mesa leads to an oxide aperture whose shape can be described as a linear combination of a circle and a square [17,46,47]. The square fraction, *s*, (ranging from 1 for a square aperture to 0 for a circular aperture) can then be used as a quantifying parameter of the degree of oxidation anisotropy [23,46].

For the richest-Sb samples ($AlAs_{0.87}Sb_{0.13}$), the observed shapes of the oxide apertures on the images of the bottom line of Fig. 2 suggests that the oxidation rates along the (110) and the (1-10) directions are no longer identical. These deformed contours thus require two anisotropy parameters to capture their shape in full and could be, in practice, effectively fitted using a linear combination between an ellipse and a rectangle. Dark vertical lines on the (white background) oxide can also be noticed at all displayed oxidation times and their presence is related to Sb segregation as it will be discussed later.

Besides the oxidation kinetics and anisotropy, another important factor to monitor is the strain given that these parameters are interlinked [26]. This is of specific relevance to this study since, as the Sb content in the AlAsSb layer increases, the strain field (initial) distribution is progressively modified because of the (in-wafer-plane) bi-axial compression of the AlAsSb layer that is imposed during the epitaxy of this material whose bulk lattice constant presents relative mismatch with the GaAs substrate ranging from 0.1% ([Sb]=0%) to 1.2% ([Sb]=13.4%). Furthermore, the oxidation process itself is known to be associated with a material volume modification that induces a (dynamic) variation of the strain field distribution. In particular, it has been established that the oxidation of AlAs layers leads to a volume contraction (usually characterized by a ~12% thickness reduction [18]) whereas the oxidation of $AlAs_{0.08}Sb_{0.92}$ layers comes with a large volume expansion (~150% thickness increase [42]). The variation of AlAsSb composition is therefore likely to lead to pronounced changes in the oxidation that are strain related. Among the various methods available to characterize the strain distribution in oxidized AlGaAs mesas [24,48,49,26,27,50], we here chose to indirectly quantify the strain by simply measuring the aperture-averaged height difference at the top surface between the (unoxidized) semiconductor and the oxide. Technically, this parameter is extracted from post-oxidation atomic force microscope surface profiles that are acquired in tapping mode at room temperature over ~20µm-wide square regions centered around ~8µm oxide apertures (see Fig. 3). It is worth pointing out at this stage that the presence of the capping layer separating the oxidized layer from the surface might lead to underestimate the embedded volume contraction.

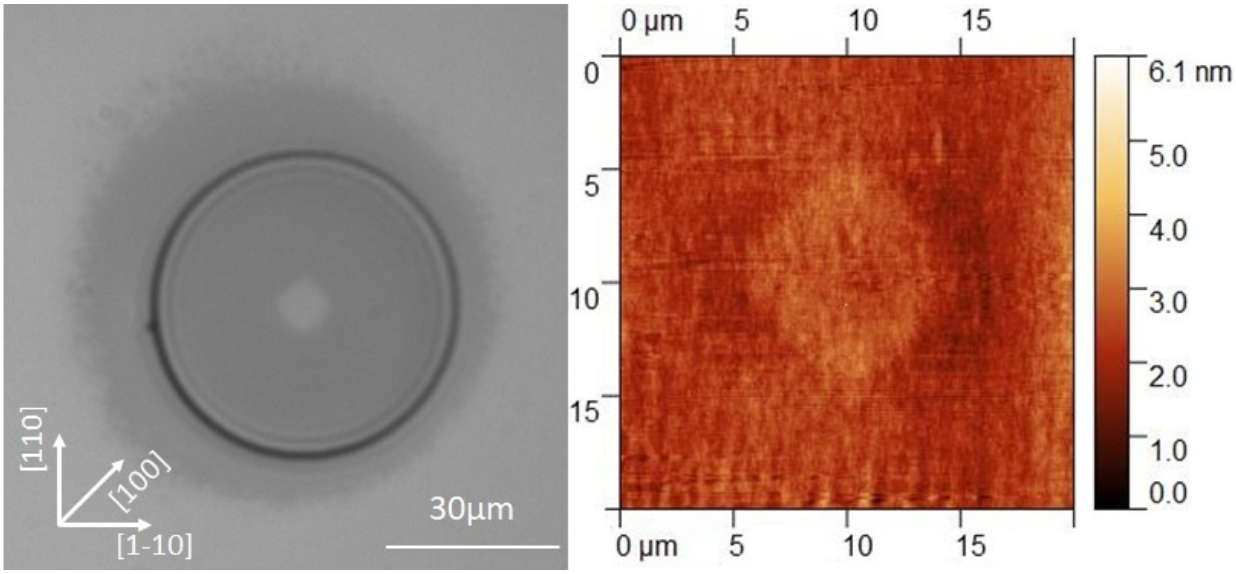

Fig. 3. Infrared image (left) of a 52µm-diameter circular mesa embedding an $AlAsSb_{6.9\%}$ layer oxidized at 380°C – 500 mbar for 63min and its atomic force microscope surface profile (right).

4. Kinetic and parametric study of the oxidation of AlAsSb

4.1 Behaviour of AlAs oxidation

To start with, oxidations of reference (AlAs-containing) samples were performed at different temperatures, sampling the standard range between 380 and 440°C. Typical examples of the extracted temporal evolutions of the aperture inner dimension and square fraction are presented in Fig. 4. Irrespective of the shape (circular or square) of the etched mesa, the oxidation progression is observed to be linear with a marginal acceleration just before aperture closure. This linear kinetics suggests that the oxidations are limited by the reactions taking place at the aperture and not by the reactant/by-products diffusion through the oxide. As illustrated in Fig. 2 and already reported for instance in [17,47], the aperture shape deforms throughout the oxidation duration. For circular etched mesas, the oxidation is observed to occur at rate very close to the fast-axis (along the (100) direction) value (see Fig. 4 and [23]). Moreover, as the oxidation progresses, the square fraction is seen to increase up to a maximum value that is reached when the aperture inner dimension gets to the size (12 µm here) below which the observation

system optical resolution restricts the ability to discriminate squares from circles. As established in [17,23], the (circular-etched-mesa) oxidation rate and the maximum square fraction constitute a sufficient basis to fully represent (four-fold-symmetric) oxidations and will therefore serve as quantifying parameters for the hereafter analysis of the oxidation of low-Sb-containing AlAsSb layers. However, full data analysis allowed to establish that the ratio of the oxidation rate along the (100) direction, $V_{(100)}$, to the one along the (110) direction, $V_{(110)}$, can be empirically related to the maximum square fraction, s_{max}, using $V_{(100)}/V_{(110)} \sim 0.74*(s_{max}-0.14)+1$.

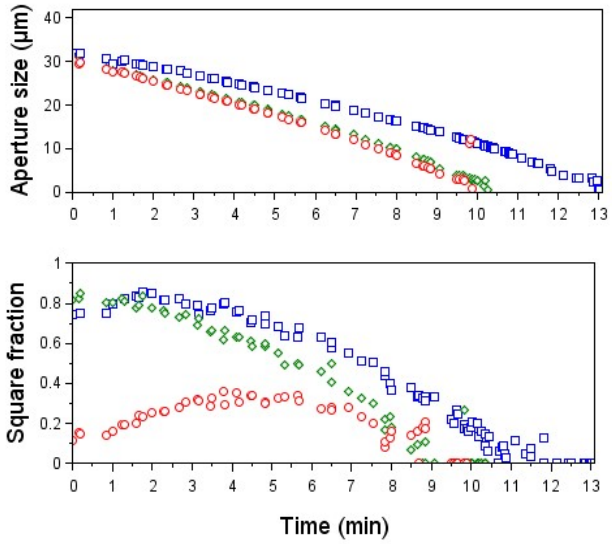

Fig. 4. Time dependence of the oxidation (420°C – 500 mbar) of AlAs from 42µm etched mesa whose shape is a circle (red), a (110)-oriented (blue) square or a (100)-oriented (green) square. The start time t=0min is taken here as the time when the aperture of the (110)-oriented square can be distinguished from its etched mesa contour.

4.2 Influence of temperature

The temperature dependence of the oxidation of AlAsSb layers is illustrated on Fig. 5 for two Sb compositions. As commonly observed, the oxidation rate increases with temperature. Since the process involves chemical reactions, the oxidation temperature dependence is often analyzed [9,10] using an Arrhenius law given by

$$V = V_0 \cdot e^{-E_a/k_B T} \qquad \text{Eq. 1}$$

where k_B is the Boltzmann constant, E_a is the activation energy

The extracted activation energies, plotted in Fig. 6, are seen to reach a minimum for a Sb concentration of 4±2%. This trend is similar to the one reported in [43] except for a shift (from 13±4% to 4±2%) in the concentration of the minimal activation energy that may originate from differences in the experimental conditions [10] (in particular in the oxidation pressure and sample preparation). As for the anisotropy, it can clearly be observed (on the central subplot of Fig. 5) that, as in the case of $Al_{0.98}Ga_{0.02}As$ layer oxidation [17], the process becomes more isotropic as the temperature increases. In the studied range of concentrations, the rise in the oxidation temperature is also found to be associated with an increase in strain, in opposition to the evolution of the anisotropy. It is however worth noting that the measured values of the semiconductor-to-oxide height step suggest a much lower oxidation shrinkage than the established value (for AlAs [18]). This artefact may be caused by the fact that the (500-nm-)thick GaAs cap separating the sample surface profile from the top oxide-interface profile may relieve part of the strain, leading to smoother recorded profiles.

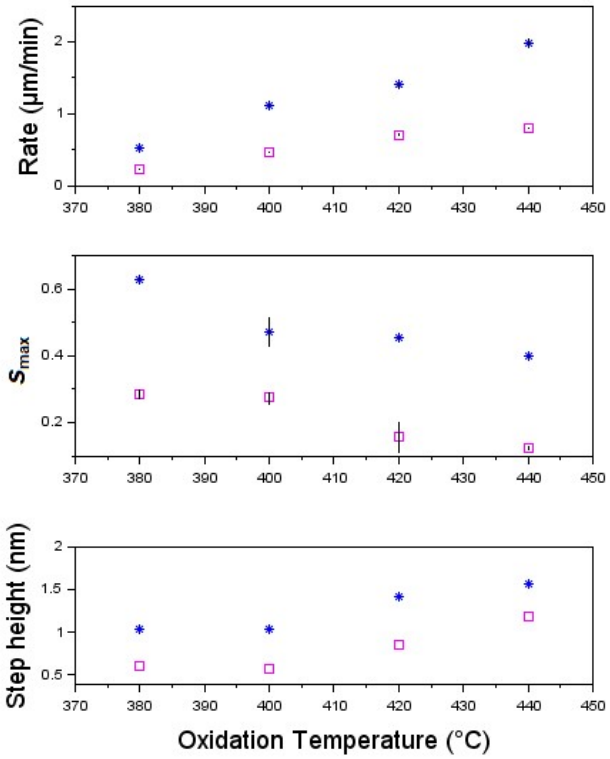

Fig. 5. Temperature dependence of AlAs (blue) $AlAs_{0.967}Sb_{0.033}$ (pink) oxidation: rate, square fraction of the aperture shape and semiconductor-to-oxide step height measured from circular mesas. Measurement error bars are indicated when relevant.

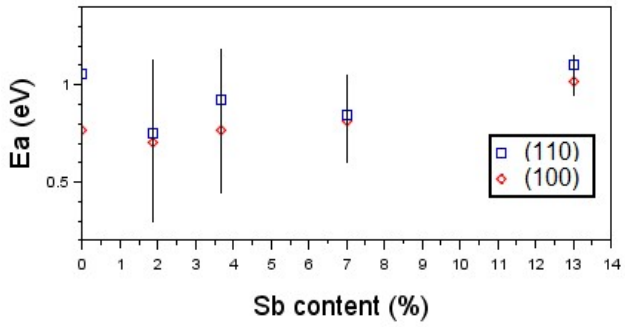

Fig. 6. Composition dependence of the oxidation rate activation energies along (110) and (100) orientations with associated error bars.

4.3 Influence of Sb composition

The analysis of the data in terms of compositional dependence is presented on Fig. 7 for compositions where four-fold symmetry oxidation is maintained (all except [Sb]=13.4%). First and foremost, the addition of Sb is found to slow the oxidation kinetics for all the studied compositions and temperatures, thereby suggesting that the reaction involving antimony is the least thermodynamically favorable of the whole reaction chain in this range of process temperatures. Furthermore, a minimum in oxidation rate is achieved in the ~2-6% Sb content range. Alloying AlAs with antimony is nevertheless observed to be more favorable than introducing gallium to maintain fast oxidation kinetics. Indeed, the oxidation of $AlAs_{1-x}Sb_x$ (x>0) compounds is, in the worst case, two times slower than the oxidation (in the same conditions) of a layer (of the same thickness) of AlAs taken as reference material while the conventionally-used $Al_{0.98}Ga_{0.02}As$ compound leads to oxidation rates that are at least 3 times slower [9] than the AlAs reference. The anisotropy is seen to follow the same trend as the oxidation rate (see Fig. 7 and Fig. 8 and additional point for [Sb]=13.4% in deduced from Fig. 11). In contrast to what has been observed for the temperature dependence, the strain here follows the same evolution as the anisotropy. This difference in behavior might be explained by the fact that the (measured) strain combines two contributions: one originating from chemically-induced volume change and the second one building up during the sample cool-down phase (from the process temperature) because of the difference in the materials thermal expansion coefficients. The results of Fig. 7 being recorded at fixed process temperatures, the measured strain evolution, derived from the AFM maps shown in Fig. 8, is thus solely representative of the variation in the reaction-induced strain. Assuming that, for a fixed process temperature, there is a linear relationship between the measured semiconductor-to-oxide step height and the volume contraction occurring upon oxidation, the inferred volume shrinkage of $AlAs_{0.967}Sb_{0.033}$ is therefore of ~7 %, a value similar to the one achieved upon oxidation of $Al_{1-x}Ga_xAs$ layers with x in the 2 to 8% range [18].

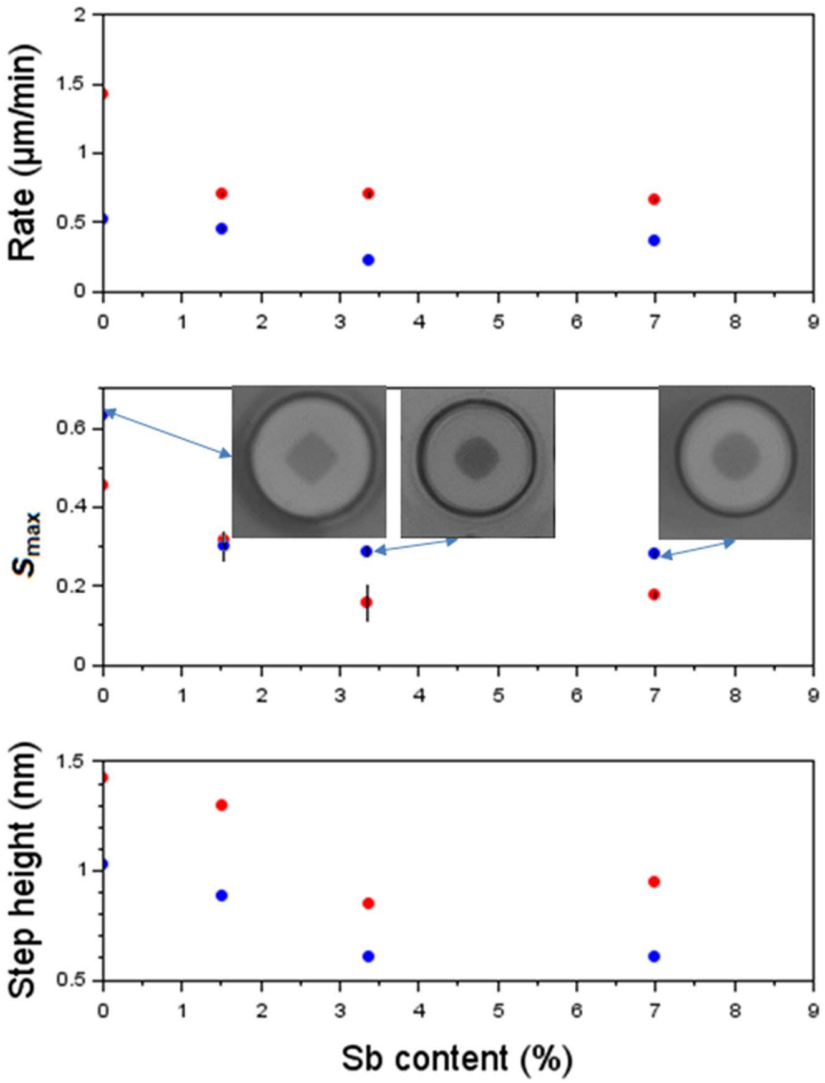

Fig. 7. Composition dependence of the oxidation characteristics measured for oxidations performed at 380 (blue) and 420°C (red). Near-infrared images with oxide extent of ~10 µm are shown as inset to give visual illustration of the Sb-content influence on the aperture anisotropy.

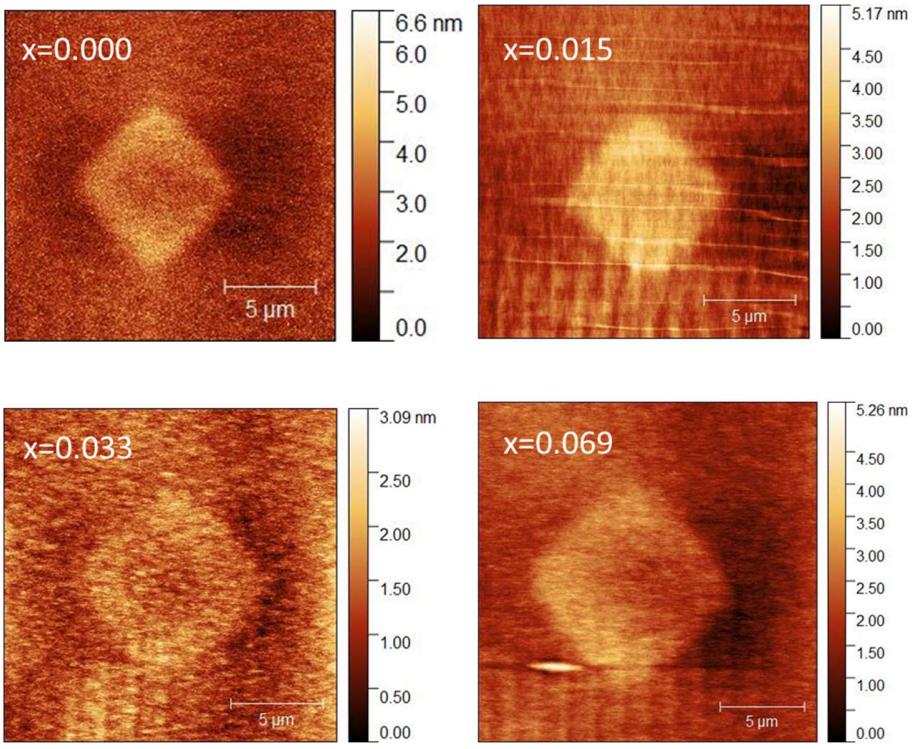

Fig. 8. AFM surface maps used to derive the oxidation strain evolution with Sb-content which is presented in the lower subplot of Fig. 7 (when the oxidations were performed at 420°C).

4.4 Influence of the oxidation chamber pressure

Since the oxidation chamber pressure modifies the supplied water concentration [51] and can also change the thermodynamics of the chemical reactions and their sequence, this study is completed by investigating the influence of this process parameter on the oxidation characteristics of $AlAs_{0.967}Sb_{0.033}$ layers. The results displayed on Fig. 9 reveal that the oxidation rate increases with pressure according to a saturating law (in blue) given by:

$$V = V_{sat}\, P/(P+P_{sat}) \qquad \text{Eq. 2}$$

with a saturated progression rate of V_{sat}=0.77 µm/min and a saturation pressure of P_{sat}=50 mbar.

Once again, the anisotropy and the strain parameters are found to follow the same behavior, both being maximum for a chamber pressure of 100 mbar and decreasing on either side. The latter observation suggests that water-supply-limited processes lead to lower volume contraction and, in turn, to more isotropic progression.

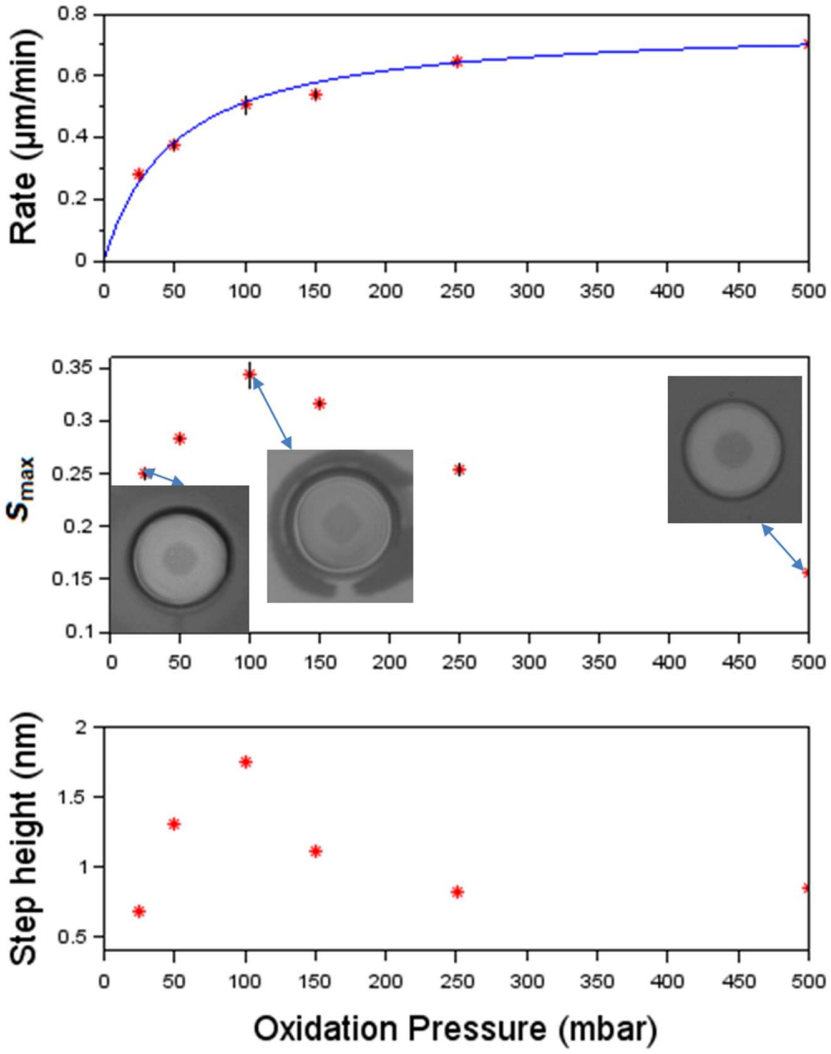

Fig. 9. Pressure-dependence of the oxidation of $AlAsSb_{3.3\%}$ layers. The curve in blue is the fitted saturating law of Eq. 2. Near-infrared images with oxide extent of ~10 µm are shown as inset to give visual illustration of the Sb-content influence on the aperture anisotropy.

4.5 High-Sb-content study

Finally, when the Sb concentration becomes too large ([Sb]=13.4% here), Sb segregation occurs as already observed in [43,44]. Experimentally, this phenomenon appears on the micro-reflectivity images with droplets emerging at the oxide aperture and subsequently migrating towards the etched mesa contour thereby creating (dark vertical) channels in the (white background) oxide region (see Fig. 2). This effect is believed to be strain-driven since the droplets arise at the location of maximum strain [27] and also because the resulting Sb removal channels are preferentially aligned with the strain-prone (110)-orientation and lead, upon aperture closure, to the drumhead patterns of Fig. 10 that look similar to the ones occasionally induced by strain during the oxidation in AlGaAs mesas [25]. This statement is further backed-up by the measured AFM surface profiles that show that the Sb-removal channels are ~20-nm-high, much taller than the ~2.2 nm semiconductor/oxide step measured along the (1-10) direction (see Fig. 11). Finally, it also worth noting that the appearance of these Sb removal channels significantly modify the oxidation rate (polar) diagram, lifting the degeneracy between the (110) and (1-10) directions, the former becoming the fastest oxidation direction with a rate ratio of ~1.26 through a combination of strain enhancement and more effective Sb removal.

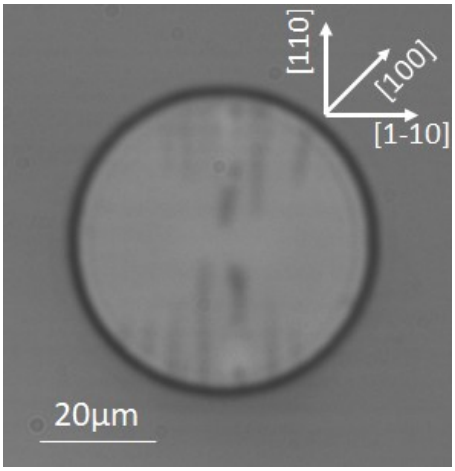

Fig. 10. Typical strain-induced drumhead pattern observed upon full oxidation (at 420°C & 500 mbar for 20 min) of $AlAsSb_{13.4\%}$-containing 52-µm-diameter circular mesa.

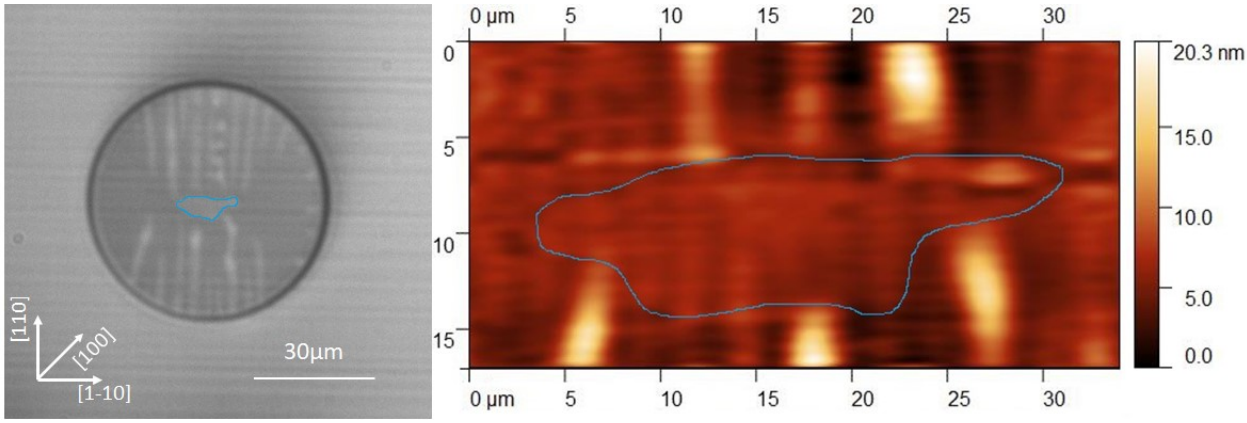

Fig. 11. Infrared image left and atomic force microscope surface profile of an oxidized $AlAsSb_{13.4\%}$ 60-µm-diameter with the oxide aperture contours highlighted in blue. The oxidation conditions are 420°C & 500 mbar for 20 min.

5. Conclusion

In this paper, the oxidation of AlAsSb nearly lattice-matched to GaAs, with several Sb concentrations up to 13.4%, has been studied in detail to gain further insight in the mechanisms ruling the influence of small amounts of Sb on the AlAs oxidation

process. In particular, it was established that for Sb content smaller than 7%, the AlAsSb layers can be oxidized without Sb segregation at a slower rate than their AlAs counterpart, indicating that Sb plays a similar role as Ga in AlGaAs oxidation but with a less drastic impact on the resulting kinetics. The investigations have also shown that oxidizing $AlAs_{0.967}Sb_{0.033}$ layers at low temperature (380°C) and in water-restricted supply (low and high pressure) leads to less-strain-baring samples and more isotropic processes, properties which can only be achieved at much higher temperatures (~480°C) with the commonly used $Al_{0.98}Ga_{0.02}As$ compounds. The above-mentioned characteristics make thin AlAsSb layers new and attractive alternatives to their AlGaAs counterparts in the fabrication of oxide-confined opto-electronics devices such as VCSELs. Additionally, the study of the oxidation of $AlAs_{0.866}Sb_{0.134}$ layers has revealed the critical role played by strain in the emergence of the detrimental Sb segregation.

Acknowledgments

This study was supported by, the ANR project "MIMICSEL" (ANR-16-CE24-0011), the ANR project "EAM-VCSELs" (ANR-19-CE24-0018) and Renatech, the French network of cleanroom facilities.

Authors declarations

The authors declare no conflicts of interest.

Data availability

The data that support the findings of this study are available from the corresponding author upon reasonable request.

References

[1] D.L. Huffaker, D.G. Deppe, K. Kumar, and T.J. Rogers, Applied Physics Letters **65**, 97 (1994).
[2] J.M. Dallesasse and D.G. Deppe, Proceedings of the IEEE **101**, 2234 (2013).
[3] J.M. Dallesasse and N. Holonyak, Journal of Applied Physics **113**, 051101 (2013).
[4] S. Calvez, G. Lafleur, A. Larrue, P.-F. Calmon, A. Arnoult, G. Almuneau, and O. Gauthier-Lafaye, IEEE Photonics Technology Letters **27**, 982 (2015).
[5] K. Welna, M. Hugues, C.P. Reardon, L. O'Faolain, M. Hopkinson, and T.F. Krauss, Photonics and Nanostructures - Fundamentals and Applications **11**, 139 (2013).

[6] A. Fiore, V. Berger, E. Rosencher, P. Bravetti, and J. Nagle, Nature **391**, 463 (1998).
[7] M. Savanier, C. Ozanam, L. Lanco, X. Lafosse, A. Andronico, I. Favero, S. Ducci, and G. Leo, Applied Physics Letters **103**, 261105 (2013).
[8] J.M. Dallesasse, N. El-Zein, N. Holonyak, K.C. Hsieh, R.D. Burnham, and R.D. Dupuis, Journal of Applied Physics **68**, 2235 (1990).
[9] K.D. Choquette, K.M. Geib, C.I. Ashby, R.D. Twesten, O. Blum, H.Q. Hou, D.M. Follstaedt, B.E. Hammons, D. Mathes, and R. Hull, Selected Topics in Quantum Electronics, IEEE Journal Of **3**, 916 (1997).
[10] W. Nakwaski, M. Wasiak, P. Ma kowiak, W. Bedyk, M. Osi ski, A. Passaseo, V. Tasco, M.T. Todaro, M.D. Vittorio, R. Joray, J.X. Chen, R.P. Stanley, and A. Fiore, Semicond. Sci. Technol. **19**, 333 (2004).
[11] K.D. Choquette, K.M. Geib, H.C. Chui, B.E. Hammons, H.Q. Hou, T.J. Drummond, and R. Hull, Applied Physics Letters **69**, 1385 (1996).
[12] I. Suárez, G. Almuneau, M. Condé, A. Arnoult, and C. Fontaine, Journal of Physics D: Applied Physics **42**, 175105 (2009).
[13] A. Fiore, Y.A. Akulova, J. Ko, E.R. Hegblom, and L.A. Coldren, IEEE Journal of Quantum Electronics **35**, 616 (1999).
[14] R. Macaluso, F. Robert, A.C. Bryce, S. Calvez, and M.D. Dawson, Semiconductor Science and Technology **18**, L12 (2003).
[15] K. Koizumi, P.O. Vaccaro, K. Fujita, M. Tateuchi, and T. Ohachi, Journal of Crystal Growth **198**, 1136 (1999).
[16] P.O. Vaccaro, K. Koizumi, K. Fujita, and T. Ohachi, Microelectronics Journal **30**, 387 (1999).
[17] G. Lafleur, G. Almuneau, A. Arnoult, S. Calvez, and H. Camon, Optical Materials Express **8**, 1788 (2018).
[18] R.D. Twesten, D.M. Follstaedt, K.D. Choquette, and R.P. Schneider, Appl. Phys. Lett. **69**, 19 (1996).
[19] T. Takamori, K. Takemasa, and T. Kamijoh, Applied Physics Letters **69**, 659 (1996).
[20] E. Guillotel, C. Langlois, F. Ghiglieno, G. Leo, and C. Ricolleau, J. Phys. D: Appl. Phys. **43**, 385302 (2010).
[21] A.C. Alonzo, X.-C. Cheng, and T.C. McGill, Journal of Applied Physics **84**, 6901 (1998).
[22] P.-C. Ku and C.J. Chang-Hasnain, IEEE Journal of Quantum Electronics **39**, 577 (2003).
[23] S. Calvez, G. Lafleur, A. Arnoult, A. Monmayrant, H. Camon, and G. Almuneau, Optical Materials Express **8**, 1762 (2018).
[24] J.P. Landesman, A. Fiore, J. Nagle, V. Berger, E. Rosencher, and P. Puech, Appl. Phys. Lett. **71**, 2520 (1997).
[25] A.C. Alonzo, X.-C. Cheng, and T.C. McGill, Journal of Applied Physics **87**, 4594 (2000).
[26] F. Chouchane, G. Almuneau, N. Cherkashin, A. Arnoult, G. Lacoste, and C. Fontaine, Applied Physics Letters **105**, 041909 (2014).
[27] F. Kießling, T. Niermann, M. Lehmann, J.-H. Schulze, A. Strittmatter, A. Schliwa, and U.W. Pohl, Phys. Rev. B **91**, 075306 (2015).
[28] F.A. Kish, S.J. Caracci, N. Holonyak, J.M. Dallesasse, A.R. Sugg, R.M. Fletcher, C.P. Kuo, T.D. Osentowski, and M.G. Craford, Appl. Phys. Lett. **59**, 354 (1991).
[29] S.J. Caracci, M.R. Krames, N. Holonyak, M.J. Ludowise, and A. Fischer-Colbrie, Journal of Applied Physics **75**, 2706 (1994).
[30] H. Gebretsadik, K. Kamath, W.-D. Zhou, P. Bhattacharya, C. Caneau, and R. Bhat, Appl. Phys. Lett. **72**, 135 (1998).
[31] B. Koley, F.G. Johnson, O. King, S.S. Saini, and M. Dagenais, Appl. Phys. Lett. **75**, 1264 (1999).
[32] P. Petit, P. Legay, G. Le Roux, G. Patriarche, G. Post, and M. Quillec, Journal of Electronic Materials **26**, L32 (1997).
[33] O. Blum, K.M. Geib, M.J. Hafich, J.F. Klem, and C.I.H. Ashby, Appl. Phys. Lett. **68**, 3129 (1996).
[34] P. Legay, P. Petit, G. Le Roux, A. Kohl, I.F.L. Dias, M. Juhel, and M. Quillec, Journal of Applied Physics **81**, 7600 (1997).

[35] S.K. Mathis, K.H.A. Lau, A.M. Andrews, E.M. Hall, G. Almuneau, E.L. Hu, and J.S. Speck, Journal of Applied Physics **89**, 2458 (2001).
[36] M.R. Peart, X. Wei, D. Borovac, W. Sun, N. Tansu, and J.J. Wierer, ACS Appl. Electron. Mater. **1**, 1367 (2019).
[37] E. Palmese, M.R. Peart, D. Borovac, R. Song, N. Tansu, and J.J. Wierer, Journal of Applied Physics **129**, 125105 (2021).
[38] O. Blum, M.J. Hafich, J.F. Klem, K. Baucom, and A. Allerman, Electron. Lett. **33**, 1097 (1997).
[39] A. Salesse, R. Hanfoug, Y. Rouillard, F. Genty, G. Almuneau, A. Baranov, C. Alibert, J. Kieffer, E. Lebeau, J.M. Luck, and L. Chusseau, Applied Surface Science **161**, 426 (2000).
[40] K. Meneou, H.C. Lin, K.Y. Cheng, J.G. Kim, and R.U. Martinelli, Journal of Applied Physics **95**, 5131 (2004).
[41] Y. Laaroussi, D. Sanchez, L. Cerutti, C. Levallois, C. Paranthoën, A. Rumeau, C. Tourte, and G. Almuneau, Electronics Letters **48**, 1616 (2012).
[42] Y. Laaroussi, J.B. Doucet, P. Fadel, L. Cerutti, I. Suarez, A. Mlayah, and G. Almuneau, Appl. Phys. Lett. **103**, 101911 (2013).
[43] P. Chavarkar, U.K. Mishra, S.K. Mathis, and J.S. Speck, Appl. Phys. Lett. **76**, 1291 (2000).
[44] A.M. Andrews, K.L. van Horn, T. Mates, and J.S. Speck, Journal of Vacuum Science & Technology A: Vacuum, Surfaces, and Films **21**, 1883 (2003).
[45] G. Almuneau, R. Bossuyt, P. Collière, L. Bouscayrol, M. Condé, I. Suarez, V. Bardinal, and C. Fontaine, Semiconductor Science and Technology **23**, 105021 (2008).
[46] S. Calvez, A. Arnoult, A. Monmayrant, H. Camon, and G. Almuneau, Semiconductor Science and Technology **34**, 015014 (2019).
[47] K. Alfaro-Bittner, R.G. Rojas, G. Lafleur, S. Calvez, G. Almuneau, M.G. Clerc, and S. Barbay, Phys. Rev. Applied **11**, 044067 (2019).
[48] R.. Keller, A. Roshko, R.. Geiss, K.. Bertness, and T.. Quinn, Microelectronic Engineering **75**, 96 (2004).
[49] F. Chouchane, G. Almuneau, O. Gauthier-Lafaye, A. Monmayrant, A. Arnoult, G. Lacoste, and C. Fontaine, Applied Physics Letters **98**, 261921 (2011).
[50] M. Mokhtari, P. Pagnod-Rossiaux, C. Levallois, F. Laruelle, D.T. Cassidy, M. Bettiati, and J.-P. Landesman, Appl. Phys. Lett. **118**, 091102 (2021).
[51] J.-S. Choe, S.-H. Park, B.-D. Choe, and H. Jeon, Semicond. Sci. Technol. **15**, L35 (2000).